





Signatures of room-temperature magnetic glassiness in zinc ferrite epitaxial thin films

Julia Lumetzberger,¹ Verena Ney ¹, Anna Zakharova ², Nieli Daffe ², Daniel Primetzhofer,³
F. Wilhelm,⁴ A. Rogalev,⁴ and Andreas Ney ^{1,*}

¹Johannes Kepler University Linz, Institute for Semiconductor and Solid State Physics, Altenberger Strasse 69, 4040 Linz, Austria

²Swiss Light Source, Paul Scherrer Institut, 5232 Villigen PSI, Switzerland

³Department of Physics and Astronomy, Ångström Laboratory, Uppsala University, Box 516, SE-751 20 Uppsala, Sweden

⁴European Synchrotron Radiation Facility, CS 40220, 38043 Grenoble Cedex, France



(Received 25 January 2023; revised 24 March 2023; accepted 4 April 2023; published 13 April 2023)

Zinc ferrite (ZnFe_2O_4) epitaxial thin films were grown by reactive magnetron sputtering on MgAl_2O_4 and Al_2O_3 substrates varying a range of preparation parameters. The resulting structural and magnetic properties were investigated using a range of experimental techniques confirming epitaxial growth of ZnFe_2O_4 with the nominal stoichiometric composition and long-range magnetic order at and above room temperature. The main preparation parameter influencing the temperature T_f of the bifurcation between $M(T)$ curves under field-cooled and zero-field-cooled conditions was found to be the growth rate of the films, while growth temperature or the Ar:O₂ ratio did not systematically influence T_f . Furthermore T_f was found to be systematically higher for MgAl_2O_4 as substrate and T_f extends to above room temperature. While in some samples T_f seems to be more likely correlated with superparamagnetism, the highest T_f occurs in ZnFe_2O_4 epitaxial films where experimental signatures of magnetic glassiness can be found. Element-selective x-ray magnetic circular dichroism measurements aim at associating the magnetic glassiness with the occurrence of a different valence state and lattice site incorporation of Fe pointing to a complex interplay of various competing magnetic interactions in ZnFe_2O_4 .

DOI: [10.1103/PhysRevB.107.144416](https://doi.org/10.1103/PhysRevB.107.144416)

I. INTRODUCTION

Zinc ferrite (ZnFe_2O_4) belongs to the crystallographic group of normal spinels of the form AB_2O_4 where in the ideal case the A cation (Zn^{2+}) exclusively occupies the tetrahedral (Td) lattice sites as Zn_{Td}^{2+} while the B cation (Fe^{3+}) is found on the octahedral (Oh) sites as Fe_{Oh}^{3+} . The magnetic properties of zinc ferrite have been under investigation for quite some time revealing a rather complex situation. In the pioneering work by Néel on the magnetic properties of spinel ferrites, zinc ferrite is already mentioned as the end point of the $3d$ series being paramagnetic at room temperature with evidence for antiferromagnetic behavior in detailed susceptibility measurements [1]. Subsequent neutron studies of the bulk material report antiferromagnetic (AFM) order with a very low Néel temperature of 9 K [2,3]. Later on it was demonstrated by magnetic neutron scattering experiments on ZnFe_2O_4 single crystals that even in perfect crystals geometrical frustration leads to an unusual magnetic behavior [4]. In particular, it was pointed out that the Fe_{Oh}^{3+} sublattice can be regarded to be similar to various pyrochlores or Laves phases which are known for their intrinsic geometrical frustration [4]. The situation becomes even more complex when defects such as inversion are considered which are expected to occur, in particular, in thin films of ZnFe_2O_4 . A partial inversion in ZnFe_2O_4 has the stoichiometric formula of $[\text{Zn}_{1-\delta}\text{Fe}_\delta]_{Td}[\text{Zn}_\delta\text{Fe}_{2-\delta}]_{Oh}\text{O}_4$, where δ denotes the degree of inversion. In the ideal case of $\delta = 0$,

i.e., no inversion, there is only the weak AFM superexchange interaction between Fe_{Oh}^{3+} which is usually denoted as J_{BB} [5] plus the geometrical frustration mentioned before [4]. J_{BB} can be held responsible for the AFM order at low temperatures in bulk single crystals. For a finite degree of inversion there is an additional, much stronger AFM superexchange interaction J_{AB} between Fe^{3+} on Td (also called A site) and Oh (or B site) sites, i.e., Fe_{Td}^{3+} and Fe_{Oh}^{3+} [5], which leads to ferrimagnetism for incomplete inversion [6]. The additional J_{AA} exchange between the Fe_{Td}^{3+} is the weakest [7]. However, if the additional Fe_{Td}^{3+} is not compensated by Zn_{Oh}^{2+} , i.e., if there is some degree of deviation from the ideal stoichiometry of ZnFe_2O_4 , some finite amount of Fe_{Oh}^{2+} has to form because of charge neutrality. This results in an additional double exchange (DE) over the Oh (or B) sites J_{BB}^{DE} between Fe_{Oh}^{3+} and Fe_{Oh}^{2+} , which results in spin canting in magnetite [5] or in nonstoichiometric ZnFe_2O_4 [6]. In many cases there are reports on some finite degree of inversion in ZnFe_2O_4 thin films and an upper limit of $\delta = 0.6$ has been found by the analysis of the magnetic moment of the Fe [8], x-ray absorption spectroscopy (XAS) [9], or via Rietveld refinement of x-ray diffraction (XRD) data [10], while it is considered to be small or absent in bulk samples [11,12]. Therefore, the magnetic order in ZnFe_2O_4 can be expected to be highly complex, especially for thin films, where the presence of various kinds of defects such as inversion and/or off-stoichiometry can be expected.

The growth of zinc ferrite in thin-film form is motivated by a range of possible applications such as gas sensors, photocatalytic disinfection, or other photocatalytic applications; see [10,13] and references therein. Besides that, zinc

*andreas.ney@jku.at

ferrite thin films can also be considered as an interesting semiconducting material in spintronics with tunable magnetic properties [5,7,14–16]. A variety of reports of different types of magnetic order in zinc ferrite can be found throughout the literature ranging from ferro(i)magnetic [5,7,16–20], to superparamagnetic [9,14,21,23,24], and to spin glass behavior [8,10,12,22,25]. Note that in some cases superparamagnetism with interparticle interactions is associated with a so-called cluster-glass behavior [8,9,12,22]. However, only a few studies report on characteristic experimental signatures of magnetic glassiness [8,10,12,22,25], while others report only temperature-dependent magnetization [$M(T)$] measurements under different field-cooling conditions which however could also be associated with superparamagnetism; e.g., [9]. Finally, the control of defects and thus the magnetic properties was reported to be experimentally achievable by varying different preparation parameters, i.e., oxygen partial pressure [7,15,20,21,24], stoichiometric composition [5], postgrowth thermal treatment [12,22,23], or deposition rate [8].

Similar to the reported types of magnetism in zinc ferrite, also the techniques for sample preparation span a wide range from pulsed laser deposition (PLD) [5,7,8,14–16,19,20,23], over reactive magnetron sputtering (RMS) [9,17,18,21,22,24] for thin-film growth, to ball milling [10] and solid state reaction [12,25] for bulklike samples. Likewise, a range of different substrates has been used for thin-film growth; among them are MgAl_2O_4 [15], c -plane Al_2O_3 [8,14], a -plane Al_2O_3 [19], SrTiO_3 [16,20,23], MgO [5,7,14], $\text{Si}(001)$ and $\text{Si}(111)$ [17,24], and glass substrates [9,18,21,22]. It is remarkable that spin glass behavior has mainly been reported for bulk ZnFe_2O_4 [4] or bulklike nanopowders [10,25] while for thin-film samples mostly a cluster glass is inferred [8,9,22]. Among the reports of cluster glass behavior only one is based on thin-film growth by PLD on single-crystalline substrates [8], while the others rely on sputtered polycrystalline ZnFe_2O_4 samples [9,22] or annealed bulklike powder samples [12] making a larger number of defects expectable, e.g., due to an intrinsically large number of grain boundaries. Finally, also the temperature range where magnetic glassiness is observed runs from below 20 K for the single-crystalline ZnFe_2O_4 in [4,25], over around 100 K for the annealed ZnFe_2O_4 nanopowders [10,12], up to 300 K for the PLD-grown ZnFe_2O_4 epitaxial films at deposition rates above 3 nm/s which drops down to below 100 K for rates below 2 nm/s [8].

Here, we report on epitaxial thin film growth of ZnFe_2O_4 by RMS on two different substrates, namely MgAl_2O_4 and c -plane Al_2O_3 . Various preparation parameters have been varied in order to control the formation of defects in a systematic way for epitaxial thin film samples. In agreement with [8] the most relevant preparation parameter is found to be the deposition rate. For high deposition rates ZnFe_2O_4 films exhibit signatures of magnetic glassiness with dominant ferromagnetic interactions up to rather high temperatures on MgAl_2O_4 substrates which is shifted to lower temperatures on Al_2O_3 substrates. In contrast, the stoichiometry on ZnFe_2O_4 is maintained throughout the sample series and also the oxygen partial pressure was found to play a minor role in the resulting magnetic properties. The signatures of magnetic glassiness are associated with a significant amount of inversion up to $\delta \sim 0.3$, corroborating earlier reports [9,10,12]. In addition,

a significant magnetic polarization of the Zn cation is found at room temperature by means of element-selective magnetometry indicating that the microscopic origin of the magnetic properties of ZnFe_2O_4 is even more complex.

II. EXPERIMENTAL DETAILS

Zinc ferrite was fabricated using reactive magnetron sputtering (RMS) from an oxide target having the nominal composition of ZnFe_2O_4 . The epitaxial thin films were grown on double-sided polished single-crystalline spinel [$\text{MgAl}_2\text{O}_4(001)$] and c -plane sapphire [$\text{Al}_2\text{O}_3(0001)$] substrates in an ultrahigh vacuum chamber with a base pressure of 4×10^{-8} mbar and a working pressure of 4×10^{-3} mbar. To determine the ideal growth parameters, the deposition temperature was varied from room temperature (RT) to 550 °C, the Ar:O₂ ratio from 10:0 to 10:0.5, and the sputtering power from 20 W to 100 W, which corresponds to a growth rate from 0.36 to 3.69 nm/min. The nominal thickness is kept at 40 nm and is controlled via a quartz crystal microbalance which is at room temperature so that the actual thickness of most of the films is by 10%–20% lower because of the elevated temperature of the substrate during growth. The structural properties of the films were investigated by x-ray diffraction (XRD) measurements with a Pananalytical X'Pert MRD recording ω - 2θ scans and symmetric as well as asymmetric reciprocal space maps (RSMs). The chemical composition was determined by ion beam analysis, i.e., Rutherford backscattering spectrometry (RBS) using a 2 MeV He⁺ primary beam at the Tandem Laboratory at Uppsala University. To disentangle the element-specific contributions, the spectra were analyzed using the SIMNRA software [26]. Details of the experimental setup are described elsewhere [27]. Furthermore, electron recoil detection (ERDA) with a primary ion beam of 36 MeV iodine ions was employed to rule out contaminations with light elements like H or C.

The magnetic properties were measured by integral superconducting quantum interference device (SQUID) magnetometry using a Quantum Design MPMS-XL5 system applying the magnetic field in the film plane. The $M(H)$ curves were recorded in a range of ± 5 T at 300 K and 2 K and $M(T)$ curves have been recorded from 2 K up to 395 K at 10 mT while warming after a cool down in 5 T (FH), under nominally zero-field-cooled conditions (ZFC), as well as while cooling down in 10 mT (field cooled, FC). Additionally, waiting time experiments were performed analogous to the ones in [28] by cooling down the sample in zero field and introducing a waiting time t_{wait} at various waiting temperatures T_{wait} which is typically 10 000 s. Then a $M(T)$ curve identical to a ZFC curve without waiting time was subsequently recorded. Subtracting these two curves represents a typical waiting time experiment for spin glasses where a so-called ZFC memory—or hole-burning—effect can be seen by a dip in the difference of the magnetization with and without waiting time around T_{wait} [28]. A second memory experiment already used before for ZnFe_2O_4 in [10] was performed in addition, in which a $M(T)$ curve is recorded under FC conditions with 10 mT and a waiting time t_{wait} at nominally zero field is inserted at several T_{wait} before the FC curve is resumed at 10 mT. Then a subsequent $M(T)$ is recorded in 10 mT while warming. The

typical signature of a spin glass in these so-called FC memory experiments is a relaxation of the magnetization at T_{wait} in the FC curve and the presence of an inflection point around T_{wait} in the subsequent $M(T)$ curve while warming [10]. Note, however, that also superparamagnets exhibit similar signatures in the FC memory experiments [29]. All $M(H)$ and $M(T)$ data were corrected for the diamagnetic background of the substrate which was determined from the $M(H)$ curves a high magnetic field at 300 K [30]. The $M(H)$ curves at 2 K for samples grown on MgAl_2O_4 had to be corrected for an additional paramagnetic contribution which was determined from a $M(H)$ measurement of bare MgAl_2O_4 from the same batch of samples. In general, zero-field conditions are referred to nominally 0.0 mT after the superconducting magnet had been reset (magnet reset option of the MPMS) and any subsequently applied magnetic field is limited to 10 mT; this assures a residual pinned magnetic field of typically 0.1 mT or less [31]. A cooling and heating rate of 1 K/min is used for all $M(T)$ measurements in both FC and ZFC memory experiments. Note that the typical frequency-dependent ac-susceptibility measurements like in [8,22,25] were not available for the used SQUID.

X-ray absorption near edge spectroscopy (XANES) and x-ray magnetic circular dichroism (XMCD) measurements in the soft x-ray regime were performed at the Xtreme beamline at the Swiss Light Source [32]. The XMCD spectra were recorded at the Fe $L_{3/2}$ and Zn $L_{3/2}$ edges at 300 K under 20° grazing incidence in total electron yield. For the Fe edges the magnetic field was set to 5 T and only the circular polarization has been switched to obtain the XMCD. For the Zn edges the direction of the magnetic field has been reversed as well to minimize artifacts. The XMCD spectra at the Fe L_3 edge are compared to simulations carried out by multiplet ligand field theory using the CTM4XAS package [33]. These simulations have been used before to determine the site occupancy and formal oxidation state of Fe and Ni in nickel ferrites [34] and Zn/Al-doped nickel ferrites [35]. For the present work the simulation parameters for $\text{Fe}_{\text{Oh}}^{2+}$, $\text{Fe}_{\text{Oh}}^{3+}$, and $\text{Fe}_{\text{Td}}^{3+}$ are identical to those in [35] and details on the simulations can be found there. The x-ray absorption near edge spectra (XANES) in the hard x-ray regime were taken at the ID12 beamline of the European Synchrotron Radiation Facility in total fluorescence yield in backscattering geometry [36]. X-ray linear dichroism (XLD) spectra at the Fe and Zn K edges were measured at 300 K as the direct difference of normalized XANES recorded under 10° grazing incidence with two orthogonal linear polarizations. A quarter wave plate was used to flip the linear polarization of the synchrotron light from vertical to horizontal; i.e., the E vector of the synchrotron light was either parallel or perpendicular to the out-of-plane (or c) axis of the ZnFe_2O_4 epitaxial film. The isotropic XANES was derived from the weighted average of the two spectra, i.e., $[2 \times \text{XANES}(E \perp c) + \text{XANES}(E \parallel c)]/3$. The x-ray magnetic circular dichroism (XMCD) measurements were taken as the direct difference of XANES spectra recorded with right and left circular polarized light under grazing incidence (15°). The XMCD spectra were recorded in an external magnetic field of up to 7 T provided by a superconducting magnet. To minimize artifacts, the external field was reversed as well.

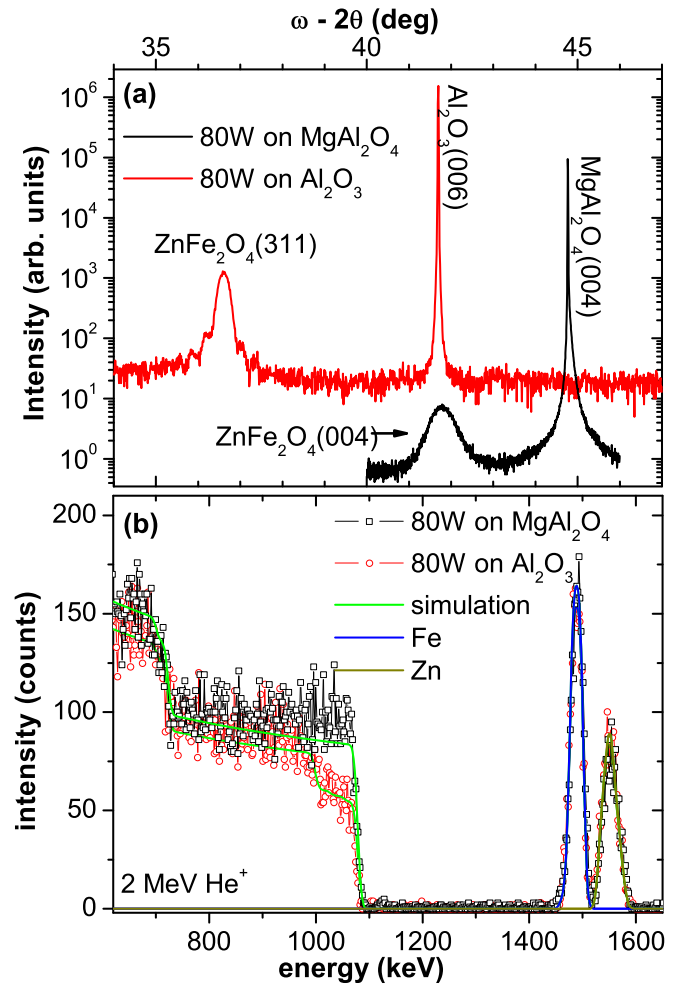


FIG. 1. (a) Structural characterization by x-ray diffraction: comparison of the symmetric ω - 2θ scans of ZnFe_2O_4 films grown at 80 W on MgAl_2O_4 (black) and Al_2O_3 (red). (b) Chemical composition determined by means of RBS spectra recorded with a 2 MeV He^+ primary ion beam of ZnFe_2O_4 films grown at 80 W on MgAl_2O_4 (black) and Al_2O_3 (red).

III. EXPERIMENTAL RESULTS

The structural properties of the ZnFe_2O_4 thin films were analyzed by symmetric ω - 2θ scans using XRD. Figure 1(a) shows a comparison of the diffractograms of zinc ferrite grown on MgAl_2O_4 and Al_2O_3 where the latter is shifted upward for clarity. The samples were grown with a nominal thickness of 40 nm at a substrate temperature of $T_S = 450^\circ\text{C}$ with an Ar:O₂ ratio of 10:0.5 and a sputtering power of 80 W. The XRD scan of the samples grown on MgAl_2O_4 exhibits a (004) reflex at $41.79^\circ \pm 0.09^\circ$ with a full width at half maximum (FWHM) of 0.6° , corresponding to a perpendicular lattice parameter $a_\perp = 8.64 \pm 0.02 \text{ \AA}$. The sample grown on Al_2O_3 exhibits the (311) reflex at 35.61° corresponding to a perpendicular lattice parameter of $a_\perp = 7.28 \pm 0.02 \text{ \AA}$. For this sample weak Laue oscillations can be seen indicating a smoother growth compared to the sample grown on MgAl_2O_4 . In addition, an asymmetric RSM along the $(\bar{1}\bar{1}5)$ plane has been recorded for a 100 nm sample grown on MgAl_2O_4 with a sputtering power of 60 W (not shown). It reveals

an in-plane lattice parameter of $a_{\parallel} = 8.32 \pm 0.05 \text{ \AA}$ which provides evidence that the film is relaxed, since the film peak does not align with the substrate peak. The reflection from the MgAl_2O_4 substrate corresponds to a lattice parameter of $a_{\text{sub}} = 8.08 \text{ \AA}$, which implies a lattice mismatch of $\sim 4.3\%$ with respect to bulk ZnFe_2O_4 ($a_0 = 8.441 \text{ \AA}$) (JCPDS card No. 82-1049). A comparison between various films grown on MgAl_2O_4 and Al_2O_3 indicates no significant difference in crystalline quality with similar FWHM despite the change in texture from (004) on MgAl_2O_4 to (311) on Al_2O_3 . No other reflexes can be found underlining highly textured growth of ZnFe_2O_4 for both substrates and the samples are devoid of other crystalline phases. Furthermore, the chemical composition of ZnFe_2O_4 on both substrates is determined using RBS. In Fig. 1(b) the RBS data of the 80 W sample grown on MgAl_2O_4 (black squares) is shown in comparison to the sample grown on Al_2O_3 (red circles). Both ZnFe_2O_4 films have no deviation from the nominal stoichiometry within the uncertainties of the measurement technique. Finally, the samples are investigated using ERDA to check for contaminations of light elements like H or C but neither element could be detected (not shown). We can therefore conclude that our ZnFe_2O_4 samples grow epitaxially on either substrate and are devoid of a significant number of secondary phases or contaminants within the detection limits of XRD and ERDA and have the nominal stoichiometric composition. This is of particular importance since also off-stoichiometry can lead to changes in the magnetic properties as reported for Zn-substituted magnetite [5].

In a first step, the magnetic properties are investigated using standard $M(H)$ curves which are shown in Fig. 2 recorded at (a) 300 K and (b) 2 K for ZnFe_2O_4 grown at 60 W on MgAl_2O_4 (black squares) and Al_2O_3 (red circles). ZnFe_2O_4 grown on Al_2O_3 has a higher magnetization of $M_s = 130 \pm 15 \text{ kA/m}$ compared to growth on MgAl_2O_4 where $M_s = 110 \pm 15 \text{ kA/m}$ at 300 K. For both samples M_s increases to above 200 kA/m at 2 K. For the $M(H)$ curves recorded at 2 K for ZnFe_2O_4 grown on MgAl_2O_4 the full squares denote the data when only the diamagnetic contribution has been subtracted. Note that in a previous publication on ZnFe_2O_4 grown on MgAl_2O_4 this apparently paramagnetic behavior has been attributed to cationic disorder of the Fe^{3+} in [15]. However, if a bare MgAl_2O_4 substrate is measured, one also measures a net-paramagnetic behavior after subtraction of the diamagnetism so that one has to attribute this paramagnetic contribution to the MgAl_2O_4 substrate itself. The open squares are the data where also the measured paramagnetic background of the bare MgAl_2O_4 has been subtracted and no obvious paramagnetic contribution of the ZnFe_2O_4 is visible any more. The insets in Fig. 2 enlarge the low-field behavior of the $M(H)$ curves. While they are virtually anhysteretic at 300 K a clear hysteresis with a coercive field of $H_c = 80 \pm 10 \text{ mT}$ is found for ZnFe_2O_4 films on either substrate. This behavior at 2 K is consistent with most of the ZnFe_2O_4 films grown on a range of different substrates reported throughout the literature reporting ferro(i)magnetism or superparamagnetism both in terms of magnetization as well as coercive field at low temperatures and clearly rules out the pure antiferromagnetic behavior of bulk ZnFe_2O_4 .

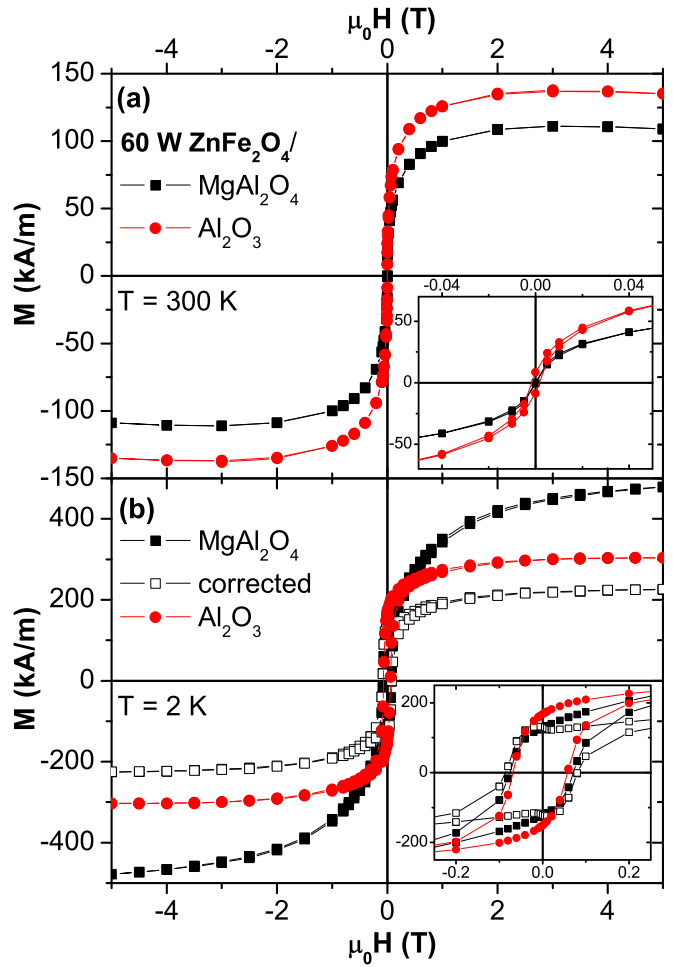


FIG. 2. SQUID measurements of $M(H)$ curves shown for the 60 W ZnFe_2O_4 grown on MgAl_2O_4 (black squares) and Al_2O_3 (red circles) at (a) 300 K and (b) at 2 K. (a) shows an $M(H)$ curve at RT (b). At 2 K the paramagnetic contribution of the MgAl_2O_4 substrate has been subtracted (open squares). The insets enlarge the measurements at low fields.

Figure 3 shows the $M(T)$ behavior recorded at 10 mT under FC conditions (full symbols) as well as after ZFC conditions (open symbols) for the ZnFe_2O_4 grown at 60 W on MgAl_2O_4 (a) and Al_2O_3 (b), i.e., an identical pair of samples to those in Fig. 2. Both samples exhibit a clear bifurcation between the FC and ZFC curves indicating a blocking or spin-freezing peak at a temperature of $T_f = 290 \text{ K}$ for $\text{ZnFe}_2\text{O}_4/\text{MgAl}_2\text{O}_4$ (a) and at $T_f = 190 \text{ K}$ for $\text{ZnFe}_2\text{O}_4/\text{Al}_2\text{O}_3$ (b). Both 60 W samples together with the two 80 W samples shown in Fig. 1 are part of a sample series where only the sputtering power and thus the deposition rate has been changed while all other growth parameters have been kept constant. In terms of magnetization as well as coercivity all samples from these series show comparable magnetic behavior. The only systematic dependency on the sputtering power is an increase of the measured T_f with increasing sputtering power. The insets in Fig. 3 show the measured T_f as a function of the sputtering power for $\text{ZnFe}_2\text{O}_4/\text{MgAl}_2\text{O}_4$ (a) as well as for $\text{ZnFe}_2\text{O}_4/\text{Al}_2\text{O}_3$ (b). Irrespective of the comparable increase with sputtering power the overall values

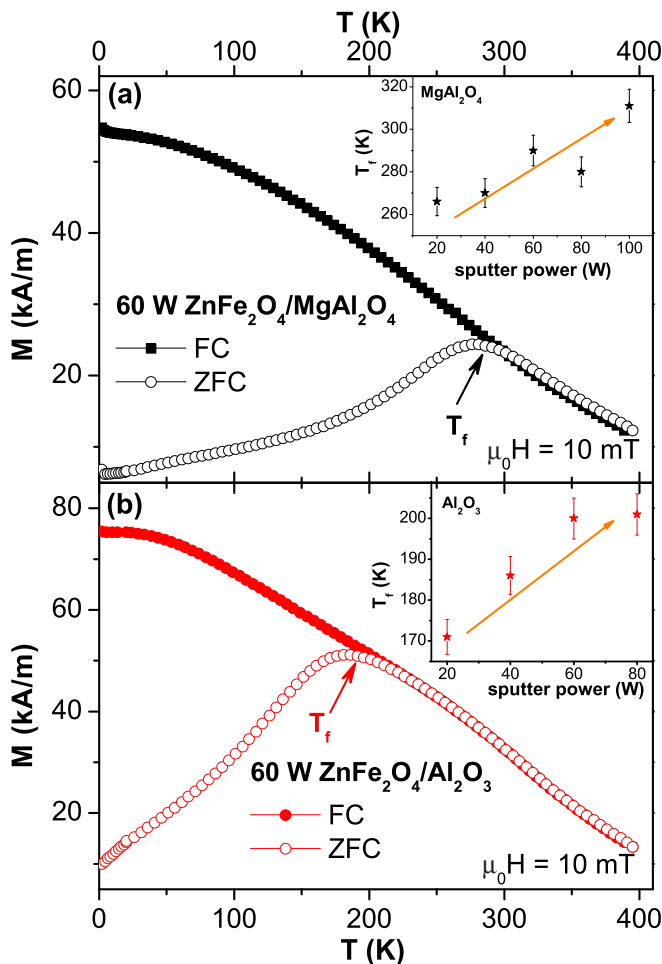


FIG. 3. $M(T)$ curves recorded at 10 mT under field-cooled (FC; full symbols) and after zero-field-cooled (ZFC; open symbols) conditions shown for the 60 W ZnFe_2O_4 grown on (a) MgAl_2O_4 (black squares) and (b) Al_2O_3 (red circles) substrates. The insets show the dependence of T_f on the sputtering power for both substrates, respectively.

of T_f are systematically lower for the Al_2O_3 substrate by about 100 K. Note that the obtained T_f for the samples grown on either substrate are well above the values usually reported for zinc ferrite [10,20,23,25]. Only in few cases the T_f is found at such elevated temperatures [8,22] and a controllable shift of T_f is only reported in [8] so far; however, the drop in T_f with decreasing deposition rate in [8] is by a factor of two more pronounced compared with the present case. Note that the power series was grown by varying the sputter power nonmonotonically so that a dependence of T_f on the growth sequence—and thus potential target degradation—can be ruled out.

In a second step, the dependence of T_f on other growth parameters will be briefly summarized. Figure 4(a) compiles the sample series as a function of the growth temperature T_{growth} from RT up to 550°C for ZnFe_2O_4 grown on MgAl_2O_4 at a sputtering power of 60 W and an Ar:O₂ ratio of 10:0.5. The XRD shows no significant changes for $T_{\text{growth}} \geq 300^\circ\text{C}$ while the sample at RT appears to be virtually amorphous. The inset shows M_s at 300 K and T_f as determined from SQUID

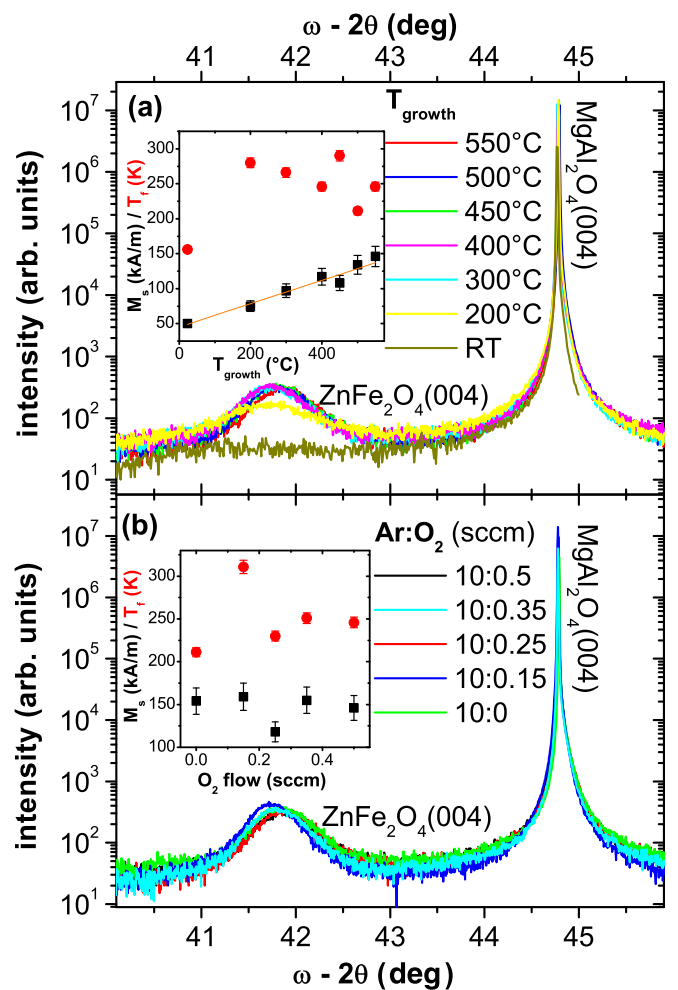


FIG. 4. (a) Structural and resulting magnetic properties as a function of the growth temperature T_{growth} for ZnFe_2O_4 grown on MgAl_2O_4 . The dependence of the identical parameters as a function of the Ar:O₂ ratio is shown in (b). M_s (black squares) and T_f (red circles) shown in the insets were extracted from SQUID measurements.

measurements analogous to Figs. 2 and 3. T_f is found to be about constant around 250 K with a slight tendency to decrease for higher T_{growth} ; the only exception is the amorphous sample at RT where T_f is clearly reduced. In contrast, M_s steadily increases with increasing T_{growth} which can be taken as an indication for an increasing amount of inversion, i.e., of $\text{Fe}_{T_d}^{3+}$ in analogy with [8,10]. However, for the present sample series this increasing M_s with T_{growth} has no obvious influence on the observed T_f . This trend is opposite to the annealing series in [10], where the amount of inversion and thus resulting M_s is decreasing with increasing annealing temperatures for nanopowdered ZnFe_2O_4 . Note that increasing T_{growth} in epitaxial growth typically leads to a decrease in actual thickness compared to the nominal one which would lead to a decrease in M_s which was calculated from the nominal thickness. On the other hand, this increase in M_s can also be associated with an increase in the order temperature which is in all cases above 400 K and thus beyond the accessible temperature range of the SQUID magnetometer and thus unknown.

A second ZnFe_2O_4 sample series was grown on MgAl_2O_4 at a sputtering power of 60 W and a fixed T_{growth} of 450°C

while varying the Ar:O₂ ratio which is compiled in Fig. 4(b). The XRD of all samples does not show any significant changes with increasing oxygen content. In the inset the resulting M_s at 300 K and T_f are shown. While M_s is independent of the Ar:O₂ ratio within error bars, T_f does not show a conclusive trend, mostly because of a rather high T_f for the sample at Ar:O₂ ratio of 10:0.15. Disregarding this, a faint increase within error bars may be inferred but there is no pronounced dependence of T_f on the Ar:O₂ ratio, especially if this is compared with the dependence on the growth rate shown in Fig. 3(a). This finding is rather interesting, since in [8] the growth rate has been associated with a deficiency in oxygen leading to an increase in T_f . However, all samples were found to be highly resistive above the GΩ range (not shown). Therefore, a significant number of oxygen vacancies can be ruled out for the entire series because the two samples grown without and with maximum oxygen partial pressure have virtually identical physical properties where the high oxygen partial pressure in RMS should safely rule out any oxygen deficiency. In turn, the dependence of T_f on the growth rate, which is consistently found in [8] and Fig. 3(a), cannot depend on the existence of oxygen vacancies for RMS-grown ZnFe₂O₄. To summarize this part, the two sample series shown in Fig. 4 underline that the relevant preparation parameter to control T_f is the sputtering power and thus growth rate, while T_{growth} and the Ar:O₂ ratio play a minor role in the resulting magnetic properties; in particular, T_f is not directly controllable via oxygen vacancies. Therefore, in the following only samples grown at an Ar:O₂ ratio of 10:0.5 and $T_{\text{growth}} = 450^\circ\text{C}$, such as those in Figs. 1–3, will be discussed further.

In a next step, the actual type of magnetic order will be determined because the reports in the literature range from ferro(i)magnetism, over superparamagnetism, to a cluster glass or spin-glass behavior. As pointed out above, M_s for the present set of samples is found to be consistent with most of the reports found throughout the literature, while the bifurcation at T_f is found at rather elevated temperatures. Figure 5(a) shows the $M(T)$ behavior recorded under FC conditions (full symbols) as well as after ZFC conditions (open symbols) for the ZnFe₂O₄ grown at 80 W on MgAl₂O₄ for an external field of 5 mT (black squares) and 10 mT (red circles). As expected T_f increases with decreasing external magnetic field which is consistent with both spin freezing as well as superparamagnetism. Note that the $M(T)$ curve under FC conditions, regardless of being similar to those reported in [8], is to a certain extent incompatible with pure spin-glass behavior, since it continues to increase with decreasing temperatures below T_f . This points toward ferro(i)magnetism, while true spin glasses are either flat with a local minimum for superspin glasses [28] or they decrease below T_f ; see [25]. Reducing the external field further to fields of 0.2 to 0.5 mT, where most of the spin glass experiments are typically carried out [25,28], T_f gets very close to the maximum attainable temperature of 400 K of the SQUID magnetometer (not shown). Therefore, all subsequent experiments are only carried out at fields of 5 mT or 10 mT to keep the maximum achievable temperature well above T_f . Note that unfortunately the SQUID does not allow to go above the magnetic order temperature which is in all cases above 400 K.

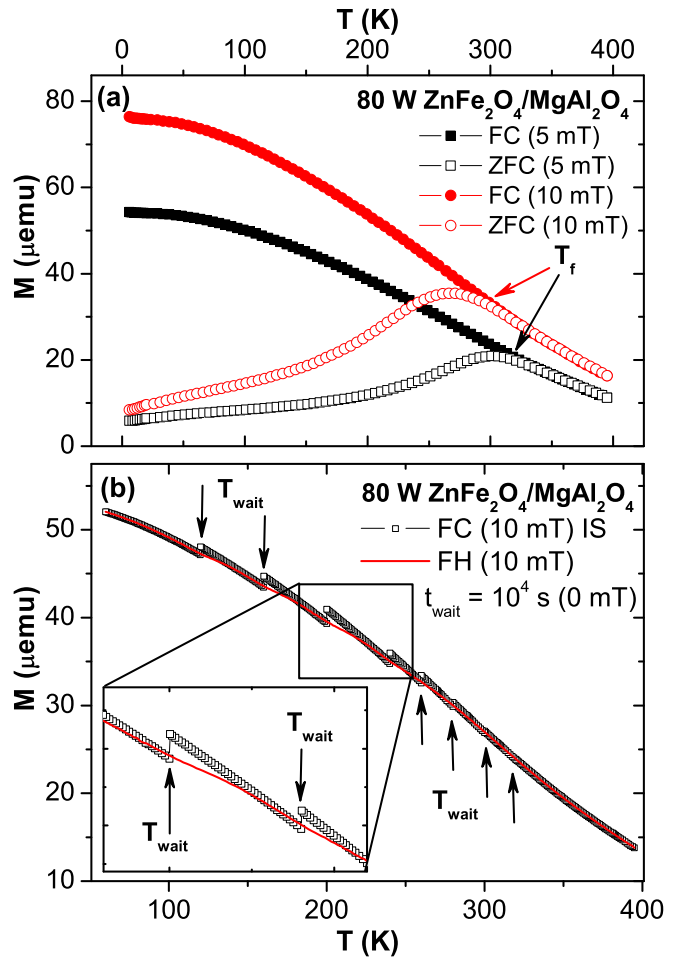


FIG. 5. (a) $M(T)$ curves of the 80 W ZnFe₂O₄ grown on MgAl₂O₄ recorded under field-cooled (FC; full symbols) and after zero-field-cooled (ZFC; open symbols) conditions at 5 mT (black squares) and 10 mT (red circles). (b) $M(T)$ curves recorded while cooling at 10 mT (FC) with intermittent stops (IS; open squares) with various T_{wait} with t_{wait} of 10 000 s marked by arrows. The $M(T)$ curve while warming is subsequently recorded at 10 mT (red line).

To get a first estimate on the existence of magnetic glassiness, the FC memory sequence used in [10] was carried out. Figure 5(b) shows the FC $M(T)$ curve recorded at 10 mT with intermittent stops (IS; open symbols) at various T_{wait} which are marked with arrows. Here the field was reduced to 0 mT for a waiting time t_{wait} of 10 000 s. Then the field was set to 10 mT again and the cooling down is resumed. Subsequently $M(T)$ is measured at 10 mT while heating at the same rate as during FC without any IS (FH; full line). In the FC curve clear steps can be seen for most T_{wait} which are most pronounced just below the maximum of the ZFC curve in Fig. 5(a), i.e., also below T_f , while they are virtually absent above T_f . Note that in Fig. 5 we show the magnetic data in emu to demonstrate the absolute size of the steps in comparison to the detection limit of the SQUID of $2\text{--}4 \times 10^{-7}$ emu [30,31]. These steps demonstrate magnetic relaxation during t_{wait} . More important, the subsequent FH curve shows clear inflection points around T_{wait} , and the inset enlarges the two most prominent ones. Therefore, there is the first

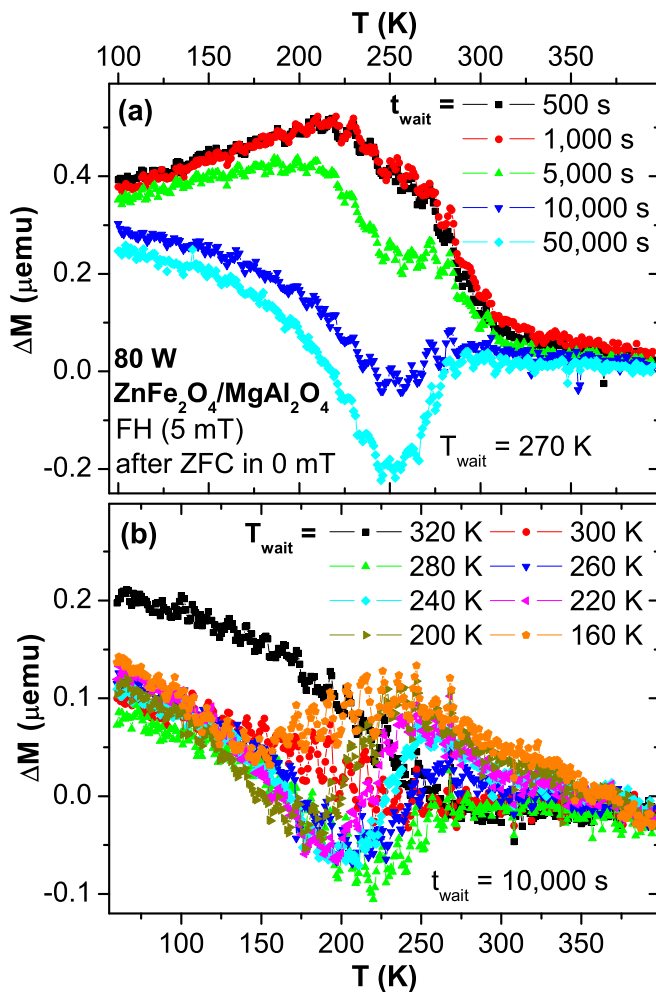


FIG. 6. Characteristic hole-burning experiment for the 80 W ZnFe_2O_4 sample grown on MgAl_2O_4 . (a) shows the dependence on the waiting time t_{wait} for a fixed waiting temperature T_{wait} of 270 K while (b) shows the dependence on T_{wait} for a fixed t_{wait} of 10 000 s.

experimental evidence for magnetic glassiness in epitaxial ZnFe_2O_4 analogous to ZnFe_2O_4 nanopowders in [10]; however, this glassiness extends to rather high temperatures which are only comparable to those reported in [8]. A caveat is still that such a behavior can also be observed and modeled in superparamagnetic samples as discussed in detail in [29] where only subtleties in these types of FC memory sequences allow us to distinguish a superparamagnet from a superspin glass. Therefore, ZFC memory experiments are needed in addition.

Figure 6 provides additional experimental evidence for magnetic glassiness of the same sample by ZFC memory experiments adopted after [28]. Here the sample is cooled down under ZFC conditions once without any waiting time and once cooling is stopped at $T_{\text{wait}} = 270$ K for varying waiting times t_{wait} from 500 s to 50 000 s. Subsequently, an $M(T)$ curve is measured at 5 mT while warming (FH). In Fig. 6(a) the difference ΔM between the FH without and with T_{wait} is plotted for all t_{wait} . Note that ΔM is provided in emu and the visible scatter in the difference data is around $1\text{--}2 \times 10^{-8}$ emu, which demonstrates the high reproducibility of the data recorded with the SQUID magnetometer. It should

be stressed that this is only possible if the magnet is reset before the measurement to eliminate any trapped flux. In all subsequent measurements one has to avoid magnetic fields larger than 10 mT so that the nominal and actual fields are identical for all measurements within 0.1 mT between which ΔM is taken. For t_{wait} of 500 s and 1000 s an increase of ΔM below T_f is visible with a maximum around the maximum of the ZFC $M(T)$ curve; i.e., ΔM follows the shape of the ZFC curve. However, the maximum of the ZFC curve for the given experimental conditions is around 300 K while the maximum of the ΔM curve is around 225 K, i.e., shifted to lower temperatures and does not go back to zero. This low-temperature increase of ΔM is difficult to be explained in a straightforward manner, because the nominally ZFC conditions only correspond to less than 0.1 mT [31]. Therefore the difference between the ZFC with and without t_{wait} of 500 s at 270 K, i.e., below T_f , implies that the system is allowed to spend an additional 500 s close to the freezing temperature in a tiny but finite field. If one considers a superparamagnetic ensemble close to its blocking temperature this implies more time for thermally activated switching in a tiny field which imprints a tiny additional magnetization because the residual field induces a slight imbalance in the probability of switching parallel and antiparallel to it. A superparamagnetic ensemble would further imply relatively fast characteristic timescales for the switching attempts. This would be in accordance with that ΔM with t_{wait} of 500 s and 1000 s are virtually identical, because all the switching events are already done, while without t_{wait} the system is ramped through the blocking temperature with a rate of 60 s/K, so many fewer switching events can take place around the blocking temperature, where the tiny residual field is sufficient to aid the thermally activated switching events. The remaining low-temperature increase is thus the frozen-in result of more switching events close to T_f resulting in a waiting-time imprinted additional magnetization. This is further corroborated by the fact that the low-temperature increase is found to decrease with decreasing T_{wait} , i.e., a waiting further below T_f , and thus in a region with potentially slower dynamics; see Fig. 6(b). We thus infer that this low-temperature increase of ΔM is most likely to be indicative of a superparamagnetic-like behavior with relatively fast dynamics rather than classical rejuvenation effects in superferromagnets as discussed in [28].

Beyond this low-temperature increase of ΔM seen for all t_{wait} in Fig. 6(a), there is a minimum evolving with increasing t_{wait} becoming clearly visible at 5000 s and being most pronounced at 50 000 s. This is a typical characteristic of a (super)spin glass as discussed in [28,29]; however, the minimum itself is rather broad in temperature and shifted to lower temperatures compared to T_{wait} by about 20 K. This shift is also seen, irrespective of the actual T_{wait} ; see also Fig. 7(a) further below. Figure 6(b) shows ΔM curves for a fixed t_{wait} of 10 000 s for various T_{wait} . For T_{wait} above T_f no minimum is visible and only the low-temperature increase can be seen. In contrast, a clear minimum is observable which is strongest for T_{wait} of 280 K, i.e., close to T_f . For lower T_{wait} it becomes less pronounced and the minimum shifts to lower temperatures, which are however always below the respective T_{wait} ; e.g., the minimum in ΔM for T_{wait} of 160 K is at 150 K (orange pentagons). Therefore, the 80 W ZnFe_2O_4 sample

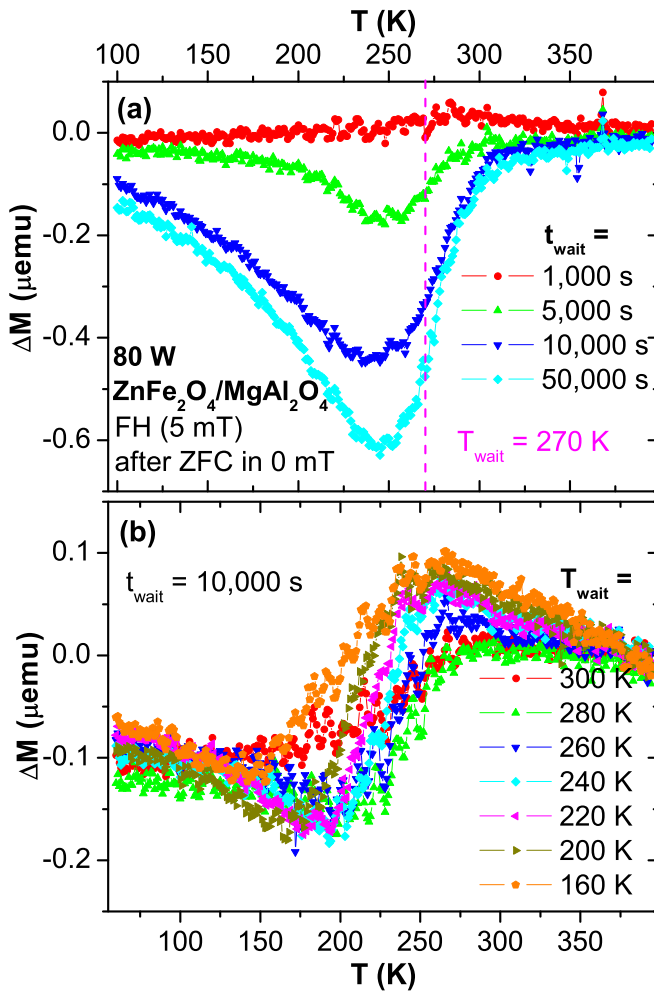


FIG. 7. Identical set of data to that in Fig. 6 for the 80 W ZnFe_2O_4 sample grown on MgAl_2O_4 for (a) varying t_{wait} for $T_{\text{wait}} = 270$ K (magenta dashed line) and (b) varying T_{wait} for $t_{\text{wait}} = 10\,000$ s; however, ΔM is taken differently (see text).

grown on MgAl_2O_4 shows most of the typical experimental characteristics of magnetic glassiness: on the one hand a FC memory effect characteristic of superparamagnets and (super)spin glasses [29] which have been reported for ZnFe_2O_4 before [10], see Fig. 5(b); on the other hand, a t_{wait} -dependent minimum is observed, which is known as the hole-burning experiment [28]. Such a hole-burning is absent in superparamagnets while it is seen in (super)spin glasses [29]. In contrast, the low-temperature increase of ΔM for short t_{wait} or T_{wait} above T_f resembles more superparamagnetic-like behavior and the increasing $M(T)$ under FC conditions hints toward dominating ferromagnetic interactions. However, we will show in the following that superparamagnetic-like behavior and magnetic glassiness may coexist.

Figure 7 provides an alternative way of presenting results identical to those in Fig. 6. In this case ΔM is taken as the difference between all data with respect to (a) $t_{\text{wait}} = 500$ s and (b) $T_{\text{wait}} = 320$ K. In other words, here $\Delta M(T)$ should only contain the magnetic glassiness since the superparamagnetic behavior—which is reflected by the low-temperature increase of ΔM seen for short t_{wait} in Fig. 6(a), or t_{wait} well above T_f

in Fig. 6(b)—is subtracted and thus only the slow, glassy dynamics can be seen. Figure 7(a) reveals that $\Delta M(T)$ of t_{wait} of 500 s and 1000 s are virtually identical, since only a zero line is visible. In other words, the fast dynamics of the superparamagnet are over/settled while the slow dynamics of the glassiness have not yet set in, both referring to the experimental accuracy. Having thus subtracted the fast dynamics the evolving dip in $\Delta M(T)$ with t_{wait} of 5000 s and higher nicely represents the remaining magnetic glassiness with its characteristic slow dynamics and ZFC memory effect. It is furthermore visible that the minimum in $\Delta M(T)$ does not align with T_{wait} which is indicated by the dashed magenta line in Fig. 7(a). T_{wait} merely appears to align with the inflection point of the high-temperature side of $\Delta M(T)$ which is also seen in the T_{wait} dependence of $\Delta M(T)$ in Fig. 7(b). Also here, the low-temperature increase of ΔM seen in Fig. 6(b) is fully removed by taking ΔM always with respect to $T_{\text{wait}} = 320$ K. Note that in Fig. 7(b) $T_{\text{wait}} = 300$ K is not nicely visible but the dip in $\Delta M(T)$ is very weak and clearly less pronounced compared to the others and in fact may only reflect the limits of reproducibility of these types of SQUID experiments; one should keep in mind that two ZFC $M(T)$ curves like in Fig. 5(a) are subtracted from each other; i.e., the signal size, and thus the relative accuracy, of each data point varies (slightly) over the entire T range which can easily affect difference signals of the order of 1×10^{-7} emu. Nevertheless, Figs. 6 and 7 nicely demonstrate that in ZnFe_2O_4 superparamagnetic-like and glassy behavior coexist and can be separated from each other. This is quite remarkable, since an epitaxial film of ZnFe_2O_4 is structurally quite distinct from a superparamagnetic ensemble like horse-spleen ferritin or a superspin glass like a dense ensemble like Fe_3N nanoparticles which were both investigated in [29]. Yet, ZnFe_2O_4 epitaxial thin films exhibit both types of magnetic order at the same time. Therefore, the observed magnetic glassiness appears to be similar to that reported in [8], which was associated with a cluster class, i.e., a superparamagnetic-like ensemble with (frustrated) intercluster interactions. However, these interactions have to be inhomogeneous and disordered throughout the sample and in contrast to the nanopowder in [10] they have no obvious structural origin. One has to therefore conclude that they stem from local variations of the cation distribution, i.e., from chemical or A/B disorder, and thus they crucially depend on a finite amount of inversion. This in turn also explains why highly crystalline bulk ZnFe_2O_4 samples with little or no inversion in [2–4,25] exhibit quite different magnetic properties.

Since we have seen that T_f is a function of the growth power during the sputtering process, the two power series of ZnFe_2O_4 samples grown on MgAl_2O_4 and Al_2O_3 shall be directly compared. For that we have chosen to perform the hole-burning ZFC waiting experiments of Fig. 6(b) on the identical relative temperature scale for each sample. In other words, the highest and lowest temperature of the $M(T)$ curves as well as T_{wait} have been chosen to be at the same relative temperature with respect to T_f to assure that the samples spent comparable time spans in regions with comparable magnetization dynamics. Note that in addition the full experiment for all T_{wait} of Fig. 6(b) on an absolute temperature scale have also been performed (not shown), but the direct comparison in essence reveals the identical result. Figure 8 shows the ΔM

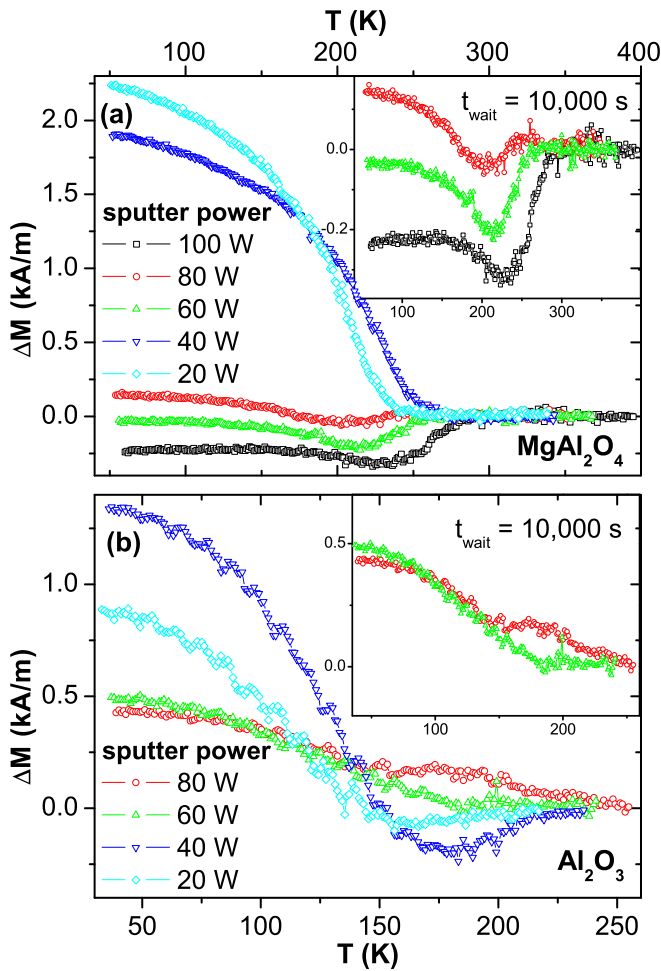


FIG. 8. Comparison of the hole-burning experiments for ZnFe_2O_4 grown on MgAl_2O_4 (a) and Al_2O_3 (b) as a function of sputter power (for details see text). The insets show the high sputter power samples only.

curves for the power series of ZnFe_2O_4 grown on MgAl_2O_4 (a) and Al_2O_3 (b) for t_{wait} of 10 000 s; the insets enlarge the samples grown at high sputtering powers. Irrespective of the substrate the samples grown at sputtering powers of 20 W and 40 W do only show the low-temperature increase of ΔM , i.e., mostly superparamagnetic-like behavior; for ZnFe_2O_4 on Al_2O_3 a faint and broad minimum is visible which however does not show a clear shift with T_{wait} or a pronounced dependence with t_{wait} . Therefore, we consider this part as inconclusive, i.e., not as clear experimental evidence for glassiness. In contrast, the samples grown at 60 W and higher all show a hole-burning behavior in the ZFC memory experiments which is pronounced for ZnFe_2O_4 on MgAl_2O_4 , see inset of Fig. 8(a), but rather weak for ZnFe_2O_4 on Al_2O_3 , for which only a faint minimum can be seen, see inset of Fig. 8(b). Therefore, in ZnFe_2O_4 on Al_2O_3 only superparamagnetic-like can be inferred and signatures of magnetic glassiness are faint and limited to high sputtering powers. This goes hand-in-hand with a more pronounced maximum in the ZFC curves, see Fig. 3(b), and an increased magnetization, see Fig. 2(a). In contrast, ZnFe_2O_4 on MgAl_2O_4 exhibits a clear transition from superparamagnetic-like behavior at low sputtering

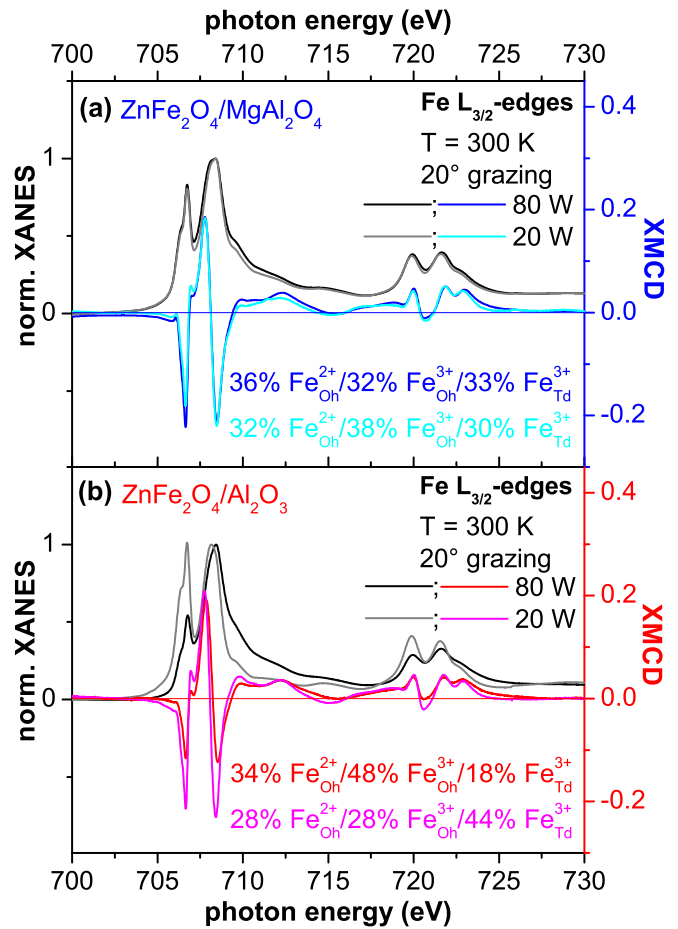


FIG. 9. Normalized XANES and XMCD spectra recorded at the $\text{Fe } L_{3/2}$ edges under grazing incidence at 300 K for the 80 W and 20 W ZnFe_2O_4 samples grown on (a) MgAl_2O_4 and (b) Al_2O_3 , respectively. The XMCD spectra have also been simulated to determine the relative amount of the individual Fe species (see text).

powers with clear signs of magnetic glassiness existing at high sputtering powers, i.e., growth rates. To ultimately clarify what causes the discrepancy in the magnetic properties for ZnFe_2O_4 grown on MgAl_2O_4 and Al_2O_3 as well as at low and high sputtering powers, the 20 W and the 80 W samples were subjected to an element-selective structural and magnetic characterization using XANES, XLD and XMCD.

Figure 9 shows the measured XANES and XMCD spectra at the $\text{Fe } L_{3/2}$ edges for ZnFe_2O_4 grown on MgAl_2O_4 (a) and Al_2O_3 (b) for the samples grown at 20 W and 80 W, respectively. The XMCD at the $\text{Fe } L_3$ edge has been also simulated by respective multiplet ligand field theory using the CTM4XAS code using parameters identical to those in [35]. In brief, the negative peaks in the XMCD spectrum are stemming from the octahedral contributions Fe_{Oh} , where $\text{Fe}_{\text{Oh}}^{2+}$ is mostly seen at lower (706.6 eV) and $\text{Fe}_{\text{Oh}}^{3+}$ at higher (708.5 eV) photon energies; the positive peak at 707.8 eV can be assigned to $\text{Fe}_{\text{Td}}^{3+}$. The experimental XMCD can be reproduced by adjusting the relative concentrations of $\text{Fe}_{\text{Oh}}^{3+}$, $\text{Fe}_{\text{Oh}}^{2+}$, and $\text{Fe}_{\text{Td}}^{3+}$ to match the experimental XMCD; the results of this are given in Fig. 9. It can be seen in Fig. 9(a) that there are no pronounced differences between the experimental XMCD

spectra of the Fe $L_{3/2}$ -edge XMCD for $\text{ZnFe}_2\text{O}_4/\text{MgAl}_2\text{O}_4$ grown at either 20 W or 80 W as well as for the respective results of the simulation. About one-third of the Fe is located on tetrahedral sites; i.e., the degree of inversion δ is around 0.3 for both sputtering powers. Also a significant amount of $\text{Fe}_{\text{Oh}}^{2+}$ is found, which would suggest a strong contribution from a $J_{\text{BB}}^{\text{DE}}$ double-exchange interaction which appears to be slightly larger for the 80 W sample which exhibits the magnetic glassiness in comparison to the 20 W sample, which only shows the superparamagnetic-like low-temperature increase of ΔM . The $\text{ZnFe}_2\text{O}_4/\text{Al}_2\text{O}_3$ samples in Fig. 9(b) exhibit a different behavior. Here the 80 W sample has a strongly reduced contribution of $\text{Fe}_{\text{Td}}^{3+}$ compared to the Fe_{Oh} compared to the 20 W sample which has the highest relative content of $\text{Fe}_{\text{Td}}^{3+}$. On the other hand, the actual positive peak in the XMCD is of identical size in both samples. It therefore appears that the XMCD intensity for the Fe_{Oh} is reduced while the amount of $\text{Fe}_{\text{Td}}^{3+}$ remains constant. This may appear as a contradiction at first sight, since the relative contents may suggest different degrees of inversion for the two samples. However, one should keep in mind that the magnetic superexchange interaction on the octahedral sites J_{BB} is weakly antiferromagnetic while double exchange leads to spin canting [5,6]. Since the magnetic order is observed up to above room temperature for all samples in this work, the J_{AB} superexchange mechanism has to play a significant role, which is consistent with a finite degree of inversion of the order of 0.3. In that light, the presence of a finite amount of inversion giving rise to $\text{Fe}_{\text{Td}}^{3+}$ is a prerequisite for magnetic order at elevated temperatures but does not play a decisive role for the presence of magnetic glassiness, since $\text{Fe}_{\text{Td}}^{3+}$ is found in all four samples while glassiness is only found in the 80 W samples, in particular in those grown on MgAl_2O_4 . In addition, the presence of $\text{Fe}_{\text{Oh}}^{2+}$ in all samples further suggests the presence of an additional $J_{\text{BB}}^{\text{DE}}$ double-exchange mechanism associated with spin canting. Here the relative amount of $\text{Fe}_{\text{Oh}}^{2+}$ increases only slightly from the 20 W sample on Al_2O_3 over 20 W on MgAl_2O_4 , 80 W on Al_2O_3 , to 80 W on MgAl_2O_4 ; i.e., it follows the trend of increasing glassiness of the samples. However, the changes are rather small and the significance of determining such small changes with multiplet ligand field simulations is limited. Obviously, there is no straightforward mechanism for the occurrence of magnetic glassiness which can be derived from the XMCD spectra at the Fe $L_{3/2}$ edges. A finite degree of inversion has to play a role but mostly for the high-order temperatures observed.

The findings at the Fe $L_{3/2}$ edges are complemented by additional experiments involving the Fe K edge. Figure 10(a) shows the normalized XANES and respective XMCD spectra recorded under grazing incidence at room temperature for the 80 W (black/blue lines) and the 20 W (red/cyan lines) ZnFe_2O_4 samples grown on MgAl_2O_4 . The overall shape of the Fe K edge of both samples is virtually identical and resembles nicely what is reported in the literature for bulk [11,37] and sputtered zinc ferrite [9]. However, a close inspection reveals that the pre-edge feature of the Fe K edge is more pronounced in the present case than for the bulk sample in [11], where the degree of inversion is much lower than for the present samples. It has been reported before that the size of the pre-edge feature depends on the degree of inversion in bulk nanopowders [38] as well as for sputtered films [9]. Likewise,

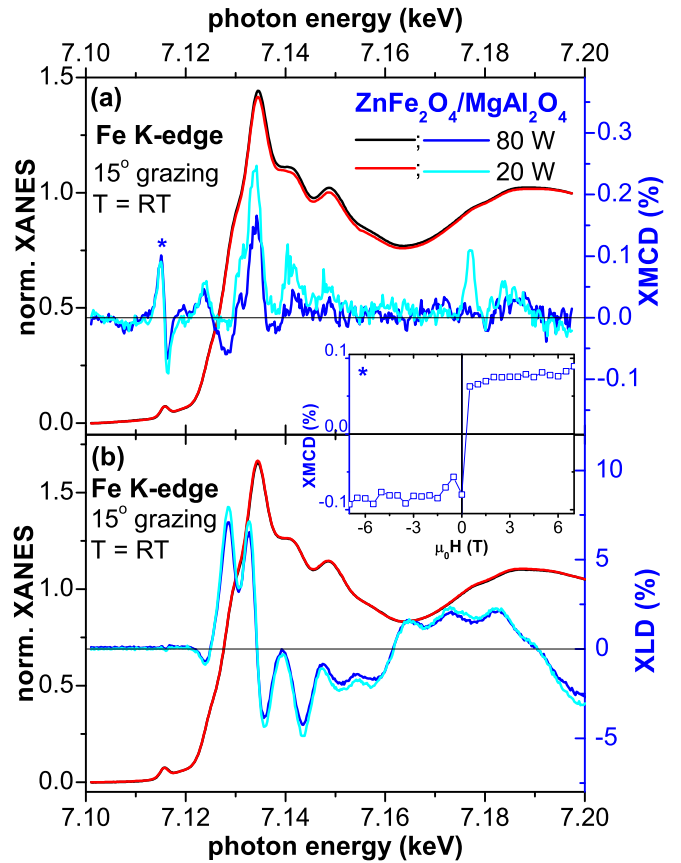


FIG. 10. (a) Normalized XANES and XMCD spectra recorded at the Fe K edge under grazing incidence at 300 K for the 80 W and 20 W ZnFe_2O_4 samples grown on MgAl_2O_4 . The field dependence of the XMCD signal recorded at the pre-edge feature (*) is shown in the inset. (b) Normalized XANES and XLD spectra at the Fe K edge for the identical pair of samples.

while in [11] no XMCD signal could be recorded, the present samples exhibit a clear XMCD signal of 0.1% with a positive and a negative peak at the pre-edge feature. Its spectral shape is comparable to the one reported in [37] for bulk nanopowders of zinc ferrite with a high degree of inversion. In that regard, the results at the Fe K edge corroborate a significant amount of inversion in the present samples independently from any additional simulations as in Fig. 9. The field dependence of the XMCD at the Fe K edge shown in the inset of Fig. 10(a) confirms the ferro(i)magnetic-like behavior seen by SQUID in Fig. 2(a) on an element-specific basis. Figure 10(b) shows the normalized XANES and respective XLD spectra of the identical pair of samples and a clear XLD signal of over 5% with pronounced peaks is visible. To the best of our knowledge XLD has not been measured before for zinc ferrite so that the obtained spectra cannot be compared to existing data and a detailed understanding of the spectral shape goes beyond the scope of this work. For the present purpose it is important to note that the XLD, which reflects the anisotropy of the unoccupied states of the absorbing atom due to its local environment, is identical in the 20 W and 80 W samples. In other words the growth rate has no significant influence on the local environment of the Fe sublattice which exhibits a net anisotropy of unknown origin; part of it may be due to

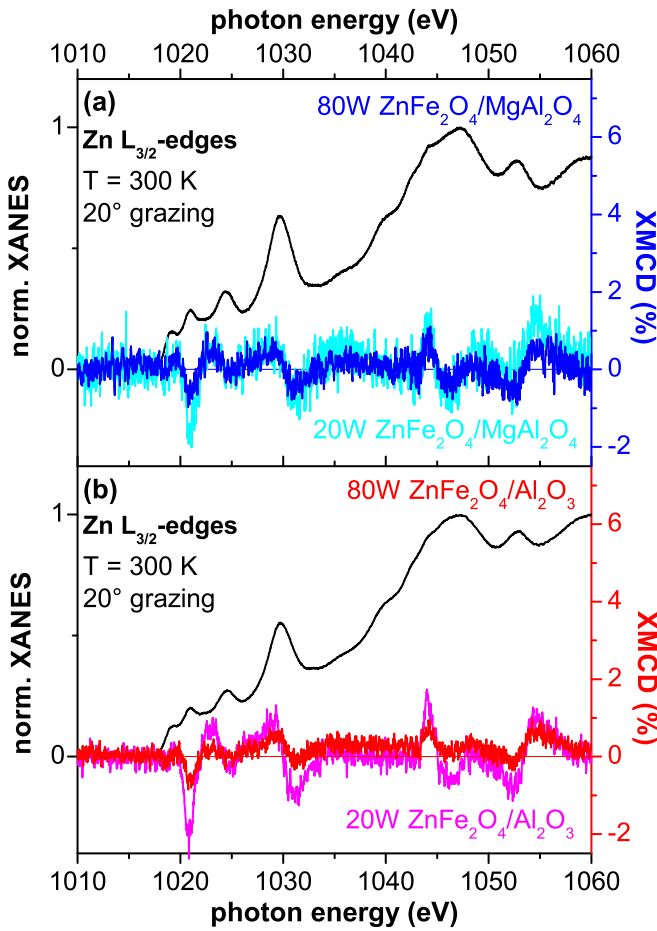


FIG. 11. Normalized XANES and XMCD spectra recorded at the Zn $L_{3/2}$ edges under grazing incidence at 300 K for the 80 W and 20 W ZnFe_2O_4 samples grown on (a) MgAl_2O_4 and (b) Al_2O_3 , respectively.

the epitaxial growth since XRD reveals different in-plane and out-of-plane lattice parameters (not shown). Note that also the XANES and XLD of the 20 W and 80 W ZnFe_2O_4 samples grown on Al_2O_3 have been measured (not shown). The overall spectral shape of the XLD is different because of the different crystallographic orientation, see Fig. 1; however, the obtained XLD spectra of both samples are identical so that also there the local environment of the Fe is identical.

Figure 11 shows the measured XANES and XMCD spectra at the Zn $L_{3/2}$ edges of the identical set of samples to those in Figs. 9 and 10. The XANES for ZnFe_2O_4 on MgAl_2O_4 in Fig. 11(a) is rather similar to the one of ZnFe_2O_4 on Al_2O_3 in (b). All four samples exhibit a finite XMCD with comparable spectral shape; all XMCD spectra were derived by reversing both helicity of the light as well as the magnetic field and it was verified that the XMCD spectrum nicely reverses with reversing external field (not shown). The size of the Zn $L_{3/2}$ -edge XMCD follows the amount of $\text{Fe}_{T_d}^{3+}$ as seen in Fig. 9; i.e., the Zn XMCD is largest for the 20 W sample on Al_2O_3 , which has the highest relative $\text{Fe}_{T_d}^{3+}$ content and it is lowest for the 20 W sample on Al_2O_3 which has the lowest relative $\text{Fe}_{T_d}^{3+}$ content. It is thus reasonable to assume that the magnetic polarization of Zn in ZnFe_2O_4 is mostly associated with $\text{Zn}_{\text{Oh}}^{2+}$. In turn, this implies that a weakly polarized cation

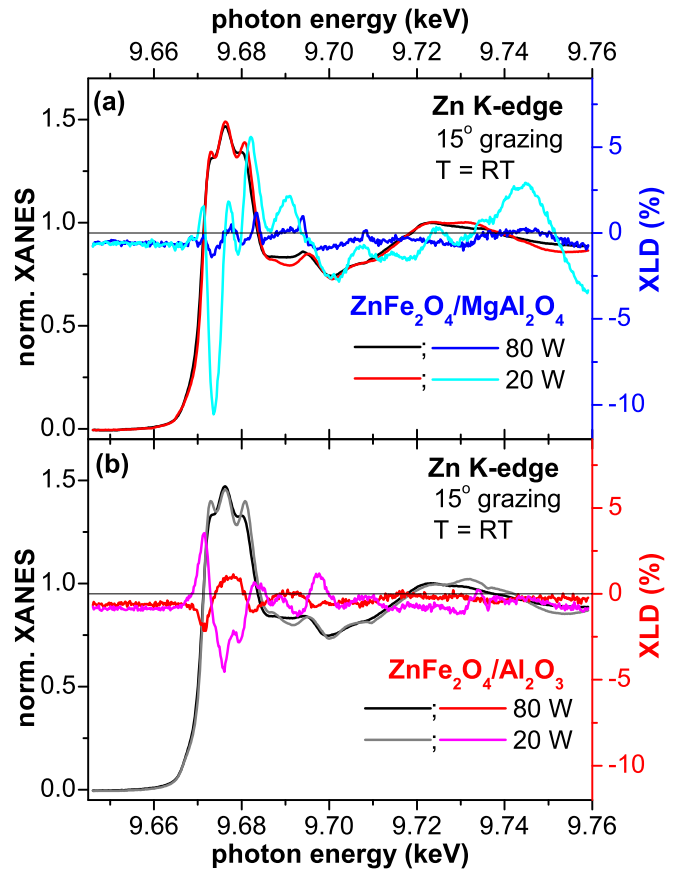


FIG. 12. Normalized XANES and XLD spectra recorded at the Zn K edge under grazing incidence at 300 K for the 80 W and 20 W ZnFe_2O_4 samples grown on (a) MgAl_2O_4 and (b) Al_2O_3 , respectively.

substitutes for a strongly polarized one thus reducing the effective exchange. This is consistent with the experimental observation that the 80 W $\text{ZnFe}_2\text{O}_4/\text{MgAl}_2\text{O}_4$ has the highest T_f and the lowest magnetic polarization of Zn while the highest Zn polarization in the 20 W $\text{ZnFe}_2\text{O}_4/\text{Al}_2\text{O}_3$ sample is associated with the lowest T_f . To verify this hypothesis, more sophisticated theoretical calculations beyond the multiplet ligand field codes is required where the individual spectroscopic signatures in the Zn $L_{3/2}$ -edge XANES and XMCD can be associated with the actual Zn species which however goes beyond the scope of this paper. Nevertheless, it is already evident that a too high degree of inversion as seen by strong magnetic polarization of the Zn together with a high relative content of $\text{Fe}_{T_d}^{3+}$ is unfavorable for both high T_f as well as magnetic glassiness, and high growth rates appear to be an experimental means to control/limit excessive inversion but at the same time assure sufficient local cationic disorder to induce magnetic glassiness.

Finally, Fig. 12 shows the normalized XANES and respective XLD spectra recorded at the Zn K edge under grazing incidence at room temperature for the 80 W and the 20 W ZnFe_2O_4 samples grown on (a) MgAl_2O_4 and (b) Al_2O_3 , respectively. The Zn K -edge XANES exhibits three distinct peaks which were observed before [9,12,38]. The relative height of the central peak has been associated with $\text{Zn}_{\text{Oh}}^{2+}$ and

is thus a spectroscopic signature of inversion which has been corroborated by simulations using density functional theory [9] or FEFF8.2 [38]. For all four samples the central peak is sufficiently pronounced to conclude a significant amount of $\text{Zn}_{\text{Oh}}^{2+}$ which is smallest for the 20 W sample grown on Al_2O_3 and comparably large for both 80 W samples. Note that in [12] magnetic glassiness has been reported for samples which all exhibited a central peak at the Zn K edge which was smaller than the first and third one, respectively, while in the present case the central peak is clearly the most intense for all four samples. The shape of the Zn K -edge XANES is most similar to the one reported for the as-deposited room-temperature sputtered zinc ferrite sample in [9] which also showed a bifurcation between $M(T)$ curves under FC and ZFC conditions similar to our findings in Fig. 3. In [9] this behavior was classified as “intrinsically frustrated magnet” which is caused by a high degree of cation disorder. In the present case we can refine these findings by the additional XLD spectra. It is remarkable that both samples grown at 20 W exhibit a clear XLD signature which is different in spectral shape for the two different substrates. Similar to the Fe sublattice some degree of (ordered) anisotropy is present. Differently from at the Fe K edge, the Zn K -edge XLD is significantly altered for the 80 W samples. For both substrates the XLD drops significantly. While for the 80 W sample on Al_2O_3 some small XLD signal with significantly altered spectral shape is still present, the XLD for the 80 W sample on MgAl_2O_4 is close to the noise level, i.e., virtually absent. Therefore, one has to conclude that the most prominent signatures of magnetic glassiness are found in a sample where the most significant difference compared to others is the absence of an XLD at the Zn K edge which is not caused by strong changes in the degree of inversion but is accompanied by a decrease in magnetic polarization of the Zn. It is therefore plausible to assign the magnetic glassiness to a strongly disordered Zn sublattice which is caused by the high growth rate but leaves the Fe sublattice mostly unaffected.

IV. DISCUSSION AND CONCLUSION

ZnFe_2O_4 epitaxial thin films have been grown on MgAl_2O_4 and Al_2O_3 substrates with varying preparation conditions. All samples were investigated with respect to their basic structural and magnetic properties and long-range magnetic order was found above room temperature for all samples. The stoichiometric composition of the samples was verified using RBS. A clear bifurcation between $M(T)$ curves under FC and ZFC conditions is found at T_f , which is systematically higher for ZnFe_2O_4 on MgAl_2O_4 by about 100 K. T_f is found to systematically increase with increasing the sputtering power and thus growth rate in agreement with [8]. The Ar:O₂ ratio was not found to influence neither T_f nor M_s in a systematic manner; increasing T_{growth} increases only M_s while T_f exhibits no systematic changes.

An in-depth study of the magnetic properties using FC as well as ZFC memory experiments reveals characteristic signatures of magnetic glassiness for samples grown at high sputter powers. The signatures are more pronounced for $\text{ZnFe}_2\text{O}_4/\text{MgAl}_2\text{O}_4$ compared to $\text{ZnFe}_2\text{O}_4/\text{Al}_2\text{O}_3$, where the signatures of magnetic glassiness are generally

weaker. For both types of samples, the signatures of glassiness are absent for lower growth rates and only the low-temperature increase of ΔM is observed which points toward superparamagnetic-like behavior. The signatures of magnetic glassiness in FC memory experiments are weak and the ZFC memory experiments shows no hole-burning effect in accordance with the expectations for superparamagnetic samples [29]. In contrast, at high growth rates, in particular for $\text{ZnFe}_2\text{O}_4/\text{MgAl}_2\text{O}_4$ ZFC memory experiments show an additional hole-burning effect which is characteristic for (super)spin glasses [28,29]. The observed magnetic properties may be described best as a cluster glass in analogy to comparable observations for epitaxial ZnFe_2O_4 in [8]. Nevertheless, the coexistence with the superparamagnetic signatures as well as the increase in $M(T)$ curves under FC conditions hint to an additional net-ferromagnetic interaction between the clusters making the magnetic properties even more complex. It has been pointed out by theory that signs of glassiness persist for spin glasses with either dominant ferro- or antiferromagnetic interactions [39]. Also in the present case the signs of magnetic glassiness such as the hole-burning effect coexist with the superparamagnetic-like signatures such as the low-temperature increase of ΔM , where the latter is dominant at lower growth rates. Turning back to the picture of a cluster glass, one has to note that T_f is determined by the size of the largest cluster [39] while smaller ones start to freeze at lower temperatures leading to a broad maximum in the ZFC $M(T)$ curves directly reflecting a broad size distribution of the clusters. Obviously, in the present case the ZnFe_2O_4 epitaxial thin films are at the border of being ferro(i)magnetically ordered while signatures of magnetic glassiness still exist up to rather elevated temperatures. Interestingly, the degree of inversion δ around 0.3 found in the present case is rather close to the percolation limit of the A sublattice where the long-range ferrimagnetic order is broken and magnetic frustration should appear as discussed in [22]. However, for a more quantitative analysis of the relevant size- and timescales frequency-dependent susceptibility measurements would be required.

An in-depth characterization based on XANES and XMCD reveals that a finite magnetic polarization at the Zn $L_{3/2}$ edges exists in all ZnFe_2O_4 samples which adds more complexity to the magnetic interactions beyond the usually discussed Fe-based exchange. At the Fe $L_{3/2}$ edges the XMCD is used to extract the relative concentrations of $\text{Fe}_{T_d}^{3+}$, $\text{Fe}_{\text{Oh}}^{3+}$, and $\text{Fe}_{\text{Oh}}^{2+}$ by means of multiplet ligand field simulations as done before [34,35]. The abundance of $\text{Fe}_{T_d}^{3+}$ correlates well with the size of the magnetic polarization of Zn and thus both can serve as a measure for the degree of inversion. For the highest degree of inversion T_f is found to be lowest and signatures of magnetic glassiness are absent. In contrast, the sample with the strongest signatures of magnetic glassiness, the 80 W $\text{ZnFe}_2\text{O}_4/\text{MgAl}_2\text{O}_4$, exhibits no significant changes in the Fe $L_{3/2}$ -edge XMCD compared to the superparamagnetic-like 20 W sample. The role of the Fe sublattice is further elucidated by XANES, XMCD, and XLD at the Fe K edges which are however hardly altered by the growth rate and the local structure around Fe is virtually identical. In contrast the XLD at the Zn K edge exhibits significant changes with growth rate and substrate. The lowest XLD and thus the largest

degree of disorder is found for the 80 W ZnFe₂O₄/MgAl₂O₄ sample with the strongest signatures of magnetic glassiness. In cases where the Zn sublattice is more ordered, the magnetic glassiness disappears and the superparamagnetic-like signatures remain. Most likely the magnetic glassiness in epitaxial ZnFe₂O₄ cannot be assigned to the actual structure of the materials like in common superparamagnets or dense nanoparticle ensembles [29] but is due to local variations of the stoichiometry, leading to an inhomogeneous local cation distribution throughout the entire sample which locally form clusters of comparable disorder with a broad size distribution which interact with neighboring ones. In summary, the local magnetic moments in ZnFe₂O₄ are disordered and frustrated due to partial inversion and a strongly disordered Zn sublattice, which leads to characteristic signatures of magnetic glassiness at rather high temperatures.

ACKNOWLEDGMENTS

J.L. gratefully acknowledges funding by Austrian Science Fund (FWF) Project No. ORD-49 at the initial stage of this work. A.Z. acknowledges the financial support by the Swiss National Science Foundation (SNSF) under Project No. 200021-169467. The x-ray absorption measurements were performed on the EPFL/PSI X-Treme beamline at the Swiss Light Source, Paul Scherrer Institut, Villigen, Switzerland. In addition, support by VR-RFI (Contracts No. 2017-006469 and No. 2019-00191) and the Swedish Foundation for Strategic Research (SSF; Contract No. RIF14-0053) supporting accelerator operation at Uppsala University is gratefully acknowledged. The research leading to this result has been supported by the RADIATE project under Grant Agreement No. 824096 from the EU Research and Innovation program HORIZON 2020.

- [1] L. Néel, *Ann. Phys.* **12**, 137 (1948).
- [2] J. M. Hastings and L. M. Corliss, *Rev. Mod. Phys.* **25**, 114 (1953).
- [3] J. M. Hastings and L. M. Corliss, *Phys. Rev.* **102**, 1460 (1956).
- [4] K. Kamazawa, Y. Tsunoda, H. Kadowaki, and K. Kohn, *Phys. Rev. B* **68**, 024412 (2003).
- [5] D. Venkateshvaran, M. Althammer, A. Nielsen, S. Geprägs, M. S. Ramachandra Rao, S. T. B. Goennenwein, M. Opel, and R. Gross, *Phys. Rev. B* **79**, 134405 (2009).
- [6] V. Zviagin, M. Grundmann, and R. Schmidt-Grund, *Phys. Status Solidi B* **257**, 1900630 (2020).
- [7] C. E. Rodríguez Torres, F. Golmar, M. Ziese, P. Esquinazi, and S. P. Heluani, *Phys. Rev. B* **84**, 064404 (2011).
- [8] Y. Yamamoto, H. Tanaka, and T. Kawai, *Jpn. J. Appl. Phys.* **40**, L545 (2001).
- [9] S. Nakashima, K. Fujita, K. Tanaka, K. Hirao, T. Yamamoto, and I. Tanaka, *Phys. Rev. B* **75**, 174443 (2007).
- [10] M. A. Cobos, P. de la Presa, I. Llorente, J. M. Alonso, A. Garcia-Escorial, P. Marin, A. Hernando, and J. A. Jimenez, *J. Phys. Chem. C* **123**, 17472 (2019).
- [11] K. Matsumoto, F. Saito, T. Toyoda, K. Ohkubo, K. Yamawaki, T. Mori, K. Hirano, M. Tanaka, and S. Sasaki, *Jpn. J. Appl. Phys.* **39**, 6089 (2000).
- [12] K. L. Salcedo Rodríguez, S. J. Stewart, P. M. Mendoza Zelis, G. A. Pasquevich, and C. E. Rodríguez Torres, *J. Alloys Compd.* **752**, 289 (2018).
- [13] D. Peeters, D. H. Taffa, M. M. Kerrigan, A. Ney, N. Jöns, D. Rogalla, S. Cwik, H.-W. Becker, M. Grafen, A. Ostendorf, C. H. Winter, S. Chakraborty, M. Wark, and A. Devi, *ACS Sustainable Chem. Eng.* **5**, 2917 (2017).
- [14] A. Marcu, T. Yanagida, K. Nagashima, H. Tananka, and T. Kawai, *J. Appl. Phys.* **102**, 023713 (2007).
- [15] F. Y. Chen, D. Spoddig, and M. Ziese, *J. Phys. D: Appl. Phys.* **41**, 205004 (2008).
- [16] A. A. Timopheev, A. M. Azevedo, N. A. Sobolev, K. Brachwitz, M. Lorenz, M. Ziese, P. Esquinazi, and M. Grundmann, *Thin Solid Films* **527**, 273 (2013).
- [17] D. Guo, C. Jiang, X. Fan, and D. Xue, *Appl. Surf. Sci.* **307**, 576 (2014).
- [18] M. Sultan and R. Singh, *J. Phys. D: Appl. Phys.* **42**, 115306 (2009).
- [19] K. Brachwitz, T. Böntgen, J. Lenzner, K. Ghosh, M. Lorenz, and M. Grundmann, *J. Phys. D: Appl. Phys.* **51**, 245003 (2018).
- [20] V. Zviagin, C. Sturm, P. D. Esquinazi, M. Grundmann, and R. Schmidt-Grund, *J. Appl. Phys.* **128**, 165702 (2020).
- [21] J. Chen, G. Srinivasan, S. Hunter, V. Suresh Babu, and M. S. Seehra, *J. Magn. Magn. Mater.* **146**, 291 (1995).
- [22] S. Nakashima, K. Fujita, K. Tanaka, and K. Hirao, *J. Phys.: Condens. Matter* **17**, 137 (2005).
- [23] Y. Kumar, I. Lorite, M. Lorenz, P. Esquinazi, and M. Grundmann, *Mater. Lett.* **195**, 89 (2017).
- [24] J. G. Monsalve, C. Ostos, E. Ramos, J. G. Ramirez, and O. Arnache, *Current Appl. Phys.* **22**, 77 (2021).
- [25] M. A. Hakim, M. Manjural Haque, M. Huc, and P. Nordblad, *Phys. B: Condens. Matter* **406**, 48 (2011).
- [26] M. Mayer, SIMNRA User's Guide, Report IPP 9/113, Max-Planck-Institut für Plasmaphysik, Garching, Germany, 1997.
- [27] M. V. Moro, R. Holeňák, L. Zendejas Medina, U. Jansson, and D. Primetzhofer, *Thin Solid Films* **686**, 137416 (2019).
- [28] S. Bedanta and W. Kleemann, *J. Phys. D: Appl. Phys.* **42**, 013001 (2009).
- [29] M. Sasaki, P. E. Jönsson, H. Takayama, and H. Mamiya, *Phys. Rev. B* **71**, 104405 (2005).
- [30] M. Sawicki, W. Stefanowicz, and A. Ney, *Semicond. Sci. Technol.* **26**, 064006 (2011).
- [31] M. Buchner, K. Höfler, B. Henne, V. Ney, and A. Ney, *J. Appl. Phys.* **124**, 161101 (2018).
- [32] C. Piamonteze, U. Flechsig, S. Rusponi, J. Dreiser, J. Heidler, M. Schmidt, R. Wetter, M. Calvi, T. Schmidt, H. Pruchova, J. Krempasky, C. Quitmann, H. Brune, and F. Nolting, *J. Synchrotron Radiat.* **19**, 661 (2012).
- [33] E. Stavitski and F. M. F. de Groot, *Micron* **41**, 687 (2010).
- [34] C. Klewe, M. Meinert, K. Kuepper, E. Arenholz, A. Gupta, J.-M. Schmalhorst, T. Kuschel, and G. Reiss, *J. Appl. Phys.* **115**, 123903 (2014).

- [35] J. Lumetzberger, M. Buchner, S. Pile, V. Ney, W. Gaderbauer, N. Daffe, M. V. Moro, D. Primetzhofer, K. Lenz, and A. Ney, *Phys. Rev. B* **102**, 054402 (2020).
- [36] A. Rogalev, F. Wilhelm, J. Goulon, and G. Goujon, in *Magnetism and Synchrotron Radiation: Towards the Fourth Generation Light Sources*, Springer Proceedings in Physics (Springer, Cham, 2013), Vol. 151, pp. 289–314.
- [37] S. J. Stewart, S. J. A. Figueroa, M. B. Sturla, R. B. Scorzelli, F. Garcia, and F. G. Requejo, *Phys. B: Condens. Matter* **389**, 155 (2007).
- [38] S. J. Stewart, S. J. A. Figueroa, J. M. Ramallo Lopez, S. G. Marchetti, J. F. Bengoa, R. J. Prado, and F. G. Requejo, *Phys. Rev. B* **75**, 073408 (2007).
- [39] B. Barbara, *Phys. Rev. Lett.* **99**, 177201 (2007).